ADVANCED FUNCTIONAL MATERIALS
www.afm-journal.de

Defect-Mediated Scintillation in Fully Inorganic Perovskites via Water-Induced 0D/3D Phase Modulation

Mario Calora, Francesco Carulli, Nadir Vanni, Antonella Giuri, Elena Ferrari, Matteo Masino, Laura Lazzarini, Francesca Rossi, Gianluca Accorsi, Anna Moliterni, Davide Altamura, Cinzia Giannini, Luca Cappelletti, Gianluca Quarta, Alberto Quaranta, Rosanna Mastria, Anna Paola Caricato, Sergio Brovelli, and Aurora Rizzo**

Scintillation detectors are essential tools in high-energy physics, medical imaging, and security, due their efficiency in converting ionizing radiation into visible light. Lead-based inorganic perovskites, particularly 3D $CsPbBr_3$, have emerged as promising next-generation scintillators due to their high photon attenuation and fast emission properties. In contrast, the 0D phase, Cs_4PbBr_6, exhibits unique emission characteristics and defect-mediated behavior, offering additional opportunities to tune scintillation performance in hybrid systems. However, the role of the 0D Cs_4PbBr_6 phase in scintillation has remained largely unexplored, and the mechanism of the emission is not well understood. Herein, a simple and reproducible synthesis of polycrystalline perovskite powders is developed with the specific scope of modulating the 3D/0D $CsPbBr_3/Cs_4PbBr_6$ phases in the samples, aiming to clarify the role of the 0D phase in the emission properties of the materials. The method relies on a solvent-antisolvent approach, in which incremental water additions selectively promote the formation of the 3D phase over the 0D one. The scintillation properties of the resulting powders are evaluated, revealing an increased scintillation yield for low water volumes used in the synthesis and an ultrafast decay time under X-ray radiation. Cathodoluminescence and temperature-dependent radioluminescence highlight defect-driven scintillation mechanisms, providing insights for future material optimization.

1. Introduction

All-inorganic perovskites have attracted attention for their outstanding thermal stability and performance in the field of optoelectronics, such as solar cells, light emitting diodes (LEDs), and high-energy radiation detectors.[1,2] Lead halide compounds show structural tunability due to the connection of the $[PbX_6]^{4-}$ (X = Cl, Br, or I) octahedra, which can form 0D isolated octahedral clusters, layers of 2D networks, and 3D corner-sharing structures (perovskites).[3–5] In all-inorganic perovskites, the small size of the Cs^+ cation enables the formation of different structural dimensionalities, which can be achieved by opportunely tuning the synthetic conditions. Particularly, the ratio of available Cs—Pb—Br precursors plays a decisive role in determining the formation of pure or mixed phases of $CsPbBr_3$ (3D), $CsPb_2Br_5$ (2D), and Cs_4PbBr_6 (0D).[6] For instance, CsBr-rich solutions lead to the formation of 0D perovskite powders, where the final product

M. Calora, G. Quarta, A. P. Caricato
Department of Mathematics and Physics "Ennio de Giorgi"
University of Salento
via per Arnesano, km 1, Lecce 73100, Italy

M. Calora, G. Quarta, A. P. Caricato, A. Rizzo
National Institute of Nuclear Physics (INFN)-Lecce Section
via per Arnesano, km 1, Lecce 73100, Italy
E-mail: aurora.rizzo@cnr.it

M. Calora, N. Vanni, A. Giuri, G. Accorsi, R. Mastria, A. Rizzo
CNR Nanotec Institute of Nanotechnology
c/o Campus Ecotekne
Via Monteroni, Lecce 73100, Italy

The ORCID identification number(s) for the author(s) of this article can be found under https://doi.org/10.1002/adfm.202512571

DOI: 10.1002/adfm.202512571

F. Carulli, L. Cappelletti, S. Brovelli
Dipartimento di Scienza dei Materiali
Università degli Studi di Milano-Bicocca
via Roberto Cozzi 55, Milano 20125, Italy
E-mail: sergio.brovelli@unimib.it

E. Ferrari, L. Lazzarini, F. Rossi
IMEM-CNR Institute
Parco Area delle Scienze 37/A, Parma 43124, Italy

M. Masino
Università degli Studi di Parma
Parco Area delle Scienze, 17/A, Parma 43124, Italy

A. Moliterni, D. Altamura, C. Giannini
CNR – Istituto di Cristallografia
Via Giovanni Amendola, 122/O, Bari 70126, Italy

A. Quaranta
Department of Industrial Engineering
via Sommarive 9, Trento 38123, Italy

A. Quaranta
INFN TIFPA
Trento Institute for Fundamental Physics and Applications
Via Sommarive 14, Povo, Trento 38123, Italy

consists of $[PbBr_6]^{4-}$ octahedra that are not connected to each other, while the Cs^+ ions are arranged in the interstitial regions, acting as an ionic insulator. Differently from the extensively studied 3D $CsPbBr_3$,[7–9] the 0D Cs_4PbBr_6 has only recently attracted significant attention due to its distinctive optical properties, such as strong photoluminescence (PL) in solid form,[10] narrow emission line width, high exciton binding energy, and outstanding thermal stability.[11] These properties, together with the high-Z atomic composition, make the material ideal for ionizing radiation detectors. In fact, Cs_4PbBr_6 single crystals have demonstrated a fast response time (τ_{AVG} = 1.46 ns) to alpha particles from an ^{241}Am radiation source and high spatial resolution of 4.0 lp mm^{-1} in X-ray imaging.[12,13] Recently, Cs_4PbBr_6 perovskite powders have been demonstrated to be compatible with polymer processing technologies. Indeed, they can be incorporated as active materials into ultra-fast 3D printed plastic scintillators for X-ray detection, achieving a response time of $\tau_{AVG} \approx 1.0$ ns, which is faster than the commercial plastic scintillator EJ-228 (τ_{AVG} = 1.31 ns),[14] holding great potential for medical applications. Apart from the clear application potential, there are still unresolved aspects concerning the inherent properties of Cs_4PbBr_6 material, especially the correlation between its photophysical and structural characteristics. One of the most intriguing aspects is related to the origin of the emission of this material, which exhibits an intense emission peak in the visible region, despite its wide bandgap (≈3.9 eV).[15] The most widely accepted hypothesis is that the green emission in Cs_4PbBr_6 comes from 3D $CsPbBr_3$ impurities,[16] which are often embedded into the 0D phase, forming intrinsic defects within the bandgap.[17,18] On the other hand, the origin of the green PL has been proposed to be due to intrinsic Br-defects within the wide bandgap of Cs_4PbBr_6[19] excluding the presence of $CsPbBr_3$ impurities as confirmed by atomic-resolution transmission electron microscopy (TEM) measurements using low-beam doses in Cs_4PbBr_6 nanocrystals (NCs).[20] Another hypothesis is the formation of self-trapped excitons, which can result in a broad emission at lower energies.[21–23]

Herein, we have developed a synthetic approach for perovskite powders with tuneable 3D/0D $CsPbBr_3/Cs_4PbBr_6$ phase content through antisolvent precipitation from CsBr-$PbBr_2$ precursor solutions in dimethyl sulfoxide (DMSO). Through a comprehensive structural and photophysical characterisation, we have investigated the mechanisms leading to the strong emissive properties of the Cs_4PbBr_6 phase under optical and ionizing radiation stimulation.

In our approach, we took advantage of the excess of CsBr present in the CsBr-$PbBr_2$ precursor solutions dissolved in DMSO to promote the formation of isolated octahedra and facilitate the precipitation of the 0D phase.[24] We found that the nature of the antisolvent is a key parameter in powder precipitation and phase tuning. In particular, using a tetrahydrofuran (THF) and water mixture as antisolvent promotes the formation of a nearly pure Cs_4PbBr_6 phase with improved emission properties, thereby increasing the PL quantum yield (PLQY) of the final sample.[25] Additionally, the inclusion of an incremental amount of water in the antisolvent mixture brings either to the precipitation of a $CsPbBr_3/Cs_4PbBr_6$ mixed phase powder or the nearly complete conversion of Cs_4PbBr_6 in $CsPbBr_3$ phase. Overall, we found that varying the water content in the antisolvent mixture modulates the 3D/0D $CsPbBr_3/Cs_4PbBr_6$ phases in the perovskite powders, as confirmed by X-ray diffraction (XRD), Raman analyses, and optical characterizations. The synthetic approach is straightforward and takes advantage of the soft nature of the metal halide perovskite lattice, along with the ability to remove the highly soluble CsBr from the soft ionic framework of Cs_4PbBr_6, as also observed in Cs_4PbBr_6 perovskite NCs through the chemical deprivation of CsBr from the CsBr-rich Cs_4PbBr_6 phase.[26–28]

To understand the origins of the emission and the potential of this material as a scintillator, we investigated the emission properties of 0D–3D hybrid perovskites under X-ray excitation and compared them with PL and cathodoluminescence (CL) to elucidate the role of defect states in the scintillation process. Radioluminescence (RL) spectra revealed excitonic emission at 2.40 eV and a dominant defect-related peak (2.26–2.33 eV), which intensifies under ionizing excitation. RL decay kinetics revealed faster recombination than PL, and a scintillation yield closer to 3000 ph MeV^{-1} for the sample prepared using 3% in volume of H_2O in the antisolvent mixture. Increasing water content during synthesis deepens defect states, impacting scintillation yield and non-radiative losses as well as modulating the two phases. CL spectra closely resemble RL, reinforcing the hypothesis that ionizing excitation promotes charge localization in shallow traps, whereas optical excitation predominantly generates band-edge excitons.

2. Result and Discussions

The Cs_4PbBr_6 powders were synthesized using a solvent-antisolvent approach,[24] in which perovskite powders were quickly precipitated from a low molarity precursor solution using a mixture of THF and deionized H_2O in different volume percentages (henceforth simply indicated as %). The nature of the solvent and anti-solvent species is expected to influence the phase of the resultant material. In order to facilitate the precipitation of the 0D phase, we selected a 0.05 M solution, in which the CsBr and $PbBr_2$ precursors are dissolved in DMSO with a molar ratio of 3.75:1 respectively. In accordance with previous studies, this approach ensures that the lead octahedra are as isolated as possible and promotes the precipitation of the Cs_4PbBr_6 phase of perovskite.[25,29,30] The use of the sole THF as an antisolvent leads to the precipitation of a colorless powder, which converts into a greenish powder after 1 h of vigorous stirring. We found that the addition of water along with THF in the antisolvent mixture accelerates the precipitation process and results in powders with different colors, depending on the amount of water added, suggesting the presence of different crystal phases. The photographs of the dried powders under ambient and UV light, with varying percentages of H_2O are shown in **Figure 1a**. The perovskite powder obtained for 3% of H_2O appears greenish in color and highly emissive under UV light. As the water content in the antisolvent increases, the perovskite powders gradually turn to an orange hue, which is accompanied by a gradual decrease in UV-induced glowing. In order to understand the nature of the as-obtained microcrystalline powders, qualitative and quantitative phase analysis based on XRD data, combined with a Raman investigation, were performed. The phase identification process is carried out using the qualitative phase analysis

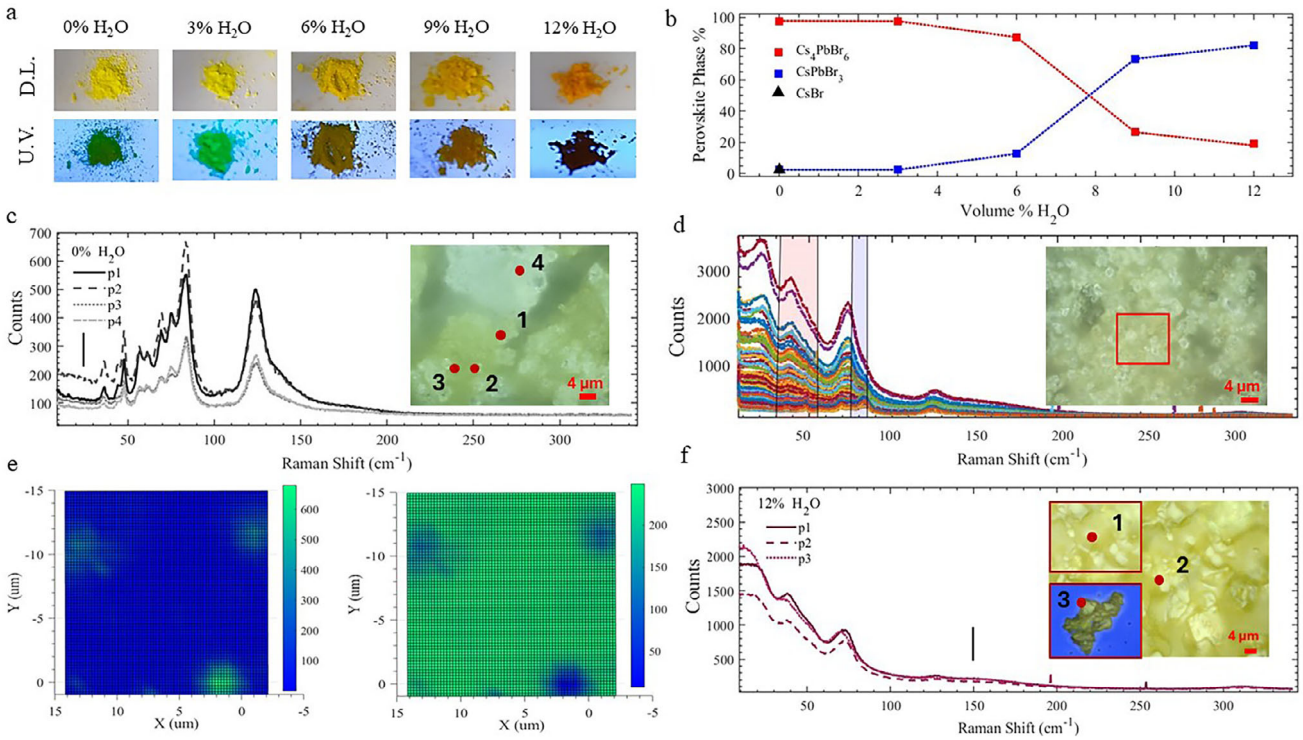

Figure 1. a) Water modulation in the Cs_4PbBr_6 samples, under daylight (D.L.) and UV light (U.V.). b) Weight percentages of perovskite phases identified in samples obtained with different percentages of water, based on quantitative analysis of the XRD patterns. c) Raman spectra of Cs_4PbBr_6 powders with 0% and the related images of the points analyzed under the optical microscope. The black line represents the Raman signal associated with the incorporation of $CsPbBr_3$ into the Cs_4PbBr_6 matrix. d) Raman spectra of Cs_4PbBr_6 6% H_2O measured on a 16 × 17 μm^2 area with 1 µm step and e) Raman intensity maps of the two species acquired from the same area highlighted in (d). f) Raman spectra of Cs_4PbBr_6 powders with 12% of H_2O in the antisolvent and the related images of the point 2 analyzed under the optical microscope. The black line represents the Raman signal associated with the incorporation of Cs_4PbBr_6 into the $CsPbBr_3$ matrix.

software QUALX2.0 by inquiring the POW_COD database,[31] a collection of known single-phase "stick" diffraction patterns built from the COD database.[32] The qualitative phase analysis suggests the following pairs of crystalline phases as the most probable ones present in the mixtures:

1) Cs_4PbBr_6 [POW_COD entry # 400–2857; Crystal system: Trigonal (hexagonal axes); $a = b = 13.7222$ Å, $c = 17.2990$ Å; space group: *R*-3*c*] and CsBr (POW_COD entry # 900–8788; Crystal system: Cubic; $a = b = c = 4.2860$ Å; space group: *Pm*-3*m*), in the case of the sample with 0% of H_2O, for which the most intense diffraction peak in the XRD pattern is located at $2\theta \approx 30.29°$, *i.e.*, the characteristic peak of Cs_4PbBr_6, revealing itself as the dominant phase[33] of the mixture, (Figure S1a, Supporting Information) while for the CsBr minority phase, a small contribution of its characteristic (110) reflection ($2\theta \approx 29.45°$) is observed.[34]
2) Cs_4PbBr_6 (POW_COD entry # 400–2857); and CsPbBr3 (POW_COD entry # 451–0745; Crystal system: Orthorhombic; $a = 8.2440$ Å, $b = 11.7351$ Å, $c = 8.1982$ Å; space group: *Pnma*), for the samples containing water. The sample containing 3% of H_2O undergoes a rapid change, resulting in the elimination of CsBr (Figure S1b, Supporting Information) and the formation of a new minority phase ($CsPbBr_3$). As the volume of water increases in the antisolvent mixture, the intensity of peaks located at $2\theta \approx 15.23°$, $2\theta \approx 21.50°$ and $2\theta \approx 30.73°$, ascribable to the 3D $CsPbBr_3$ phase,[35] increase so that $CsPbBr_3$ becomes the predominant phase for 9% and 12% of H_2O, where Cs_4PbBr_6 is now the minority phase (Figure S1c, Supporting Information).

The weight percentage of the two component phases (w1 and w2), estimated by a quantitative phase analysis (QPA) carried out on the XRD patterns (Figure S1d, Supporting Information) by the Rietveld method [36,37] using the EXPO package,[38] are provided in Table S1 (Supporting Information). It is noteworthy that the most intense diffraction peaks corresponding to the majority phases in the investigated mixtures – Cs_4PbBr_6 ($2\theta \approx 30.3°$) for the samples with 0%, 3%, and 6% H_2O, and $CsPbBr_3$ ($2\theta \approx 30.7°$) for those with 9% and 12% H_2O- likely arise from preferred orientation (PO) effects, particularly along the (101) plane. In these cases, PO effects were taken into account and corrected using the EXPO software. Notably, the diffraction peak at $2\theta \approx 30.3°$, associated with Cs_4PbBr_6, exhibits progressive broadening of the full width at half maximum (FWHM) as the H_2O content increases, except for the sample with 3% H_2O. This trend suggests either a reduction in crystallinity or a decrease in the sizes of coherent domains In contrast, the peak at $2\theta \approx 30.7°$, attributed to $CsPbBr_3$, shows a narrowing of the FWHM with increasing water content, indicating enhanced crystal growth (see Figure S1e, Supporting

Information). The weight percentages of the 0D and 3D phases are graphically represented in Figure 1b, as a function of water content in the antisolvent. The graph clearly shows that water induces phase modulation, enabling the tuning of the powder composition from nearly pure Cs_4PbBr_6 to a product with a high percentage of $CsPbBr_3$. Raman spectroscopy at room-temperature was performed using a 633 nm excitation laser on representative regions of each sample, to confirm the phase modulation induced by increasing H_2O content in the antisolvent.

Figure 1c illustrates the Raman spectra of Cs_4PbBr_6 without H_2O, which exhibits two strong modes below 50 cm^{-1}, a group of three peaks in the 70–90 cm^{-1} range, and a strong mode at ≈120 cm^{-1}. The two peaks in the low frequency region likely correspond to lattice vibrational modes associated with the translational modes of the Cs^+ ions relative to the isolated $[PbBr_6]^{4-}$ octahedra.[39] Instead, the three distinct peaks in the 70–90 cm^{-1} range are likely to be bending modes of the $[PbBr_6]^{4-}$ octahedra, which may vary depending on the crystalline environment such as a modification of Pb-Br interactions due to local distortions in the Cs_4PbBr_6 structure. The last strong peak at ≈120 cm^{-1} is probably associated with the symmetric stretching of the Pb—Br bond in the isolated $[PbBr_6]^{4-}$ octahedra.[40] It is crucial to note that these distinct peaks are indicative of an isolated structure, such as that of the 0D Cs_4PbBr_6 configuration, where the octahedra are not connected to each other. However, an increase in spectral weight below 50 cm^{-1} (e.g., point 1 and 2 in Figure 1c) can be attributed to lattice defects, such as $CsPbBr_3$ NCs, which are not detected by XRD analyses.[41] Additionally, we observe that the increase in spectral weight below 50 cm^{-1} (marked with a vertical line) systematically correlates with the emergence of a shoulder between 130 and 160 cm^{-1}. This shoulder could arise from the overlap of vibrational modes originating from both Cs_4PbBr_6 and $CsPbBr_3$ phases. The image acquired under the microscope of the sample reveals a white Cs_4PbBr_6 major phase with 1–4 µm size grains and a small amount of orange µm-sized $CsPbBr_3$ grains. A similar trend is evident in the sample with 3% H_2O, where the Cs_4PbBr_6 grains are of an identical size to those observed in the previous sample and represent the predominant phase (Figure S2a,b, Supporting Information). Even in the Raman spectrum there is a similar trend, with the broadening and doubling of some peaks (in the range associated to translational mode of the Cs^+ and bending modes of the $[PbBr_6]^{4-}$), suggesting structural changes. A greater separation is noted in the peaks between 70 and 90 cm^{-1} due to an influence on the vibrations of the $[PbBr_6]^{4-}$ octahedra, modifying their bending dynamics, and the peak at ≈120 cm^{-1} appears to be more intense and shifted respect the sample without H_2O due to a slight distortion of the local structure, which modifies the rigidity of the Pb—Br bonds. In fact, the antisymmetric stretching mode of the Pb—Br bonds in the isolated $[PbBr_6]^{4-}$ octahedra can be identified (105–110 cm^{-1}), which is accompanied by a broadening of the shoulder in the 150–200 cm^{-1} region, likely due to lattice disorder or overlapping vibrational contributions. This may be associated with the intrusion of $CsPbBr_3$ defects confirmed by the signal at 310 cm^{-1} already found in previous works.[39–41] It is postulated that the latter is embedded at low concentrations in the predominant phase, and this is also confirmed from the XRD analysis. In the sample containing 6% H_2O, a heterogeneous population of grains measuring 1–4 µm is observed, belonging to both the Cs_4PbBr_6 and $CsPbBr_3$ phases (Figure 1d). This has repercussions on the Raman analysis of the Cs_4PbBr_6 6% H_2O sample where the peaks are more intense and wider below 100 cm^{-1} suggesting a structural change. Figure 1e illustrates the color map of the highlighted region in Figure 1d, obtained by integrating the Raman signal over two characteristic shift intervals corresponding to $CsPbBr_3$ and Cs_4PbBr_6, respectively.

It is interesting to note that the intensity of the $CsPbBr_3$ raman signal is consistently higher than that of Cs_4PbBr_6, and the two signals exhibit a complementary spatial distribution. This behavior suggests the coexistence of the two polycrystalline phases within the samples. As previously indicated by XRD analyses, an increase in water content above 9% results in the formation of the $CsPbBr_3$ phase as the predominant phase. Microscopic observations reveal the presence of larger grains, ≈4–10 µm in size of $CsPbBr_3$ (Figure S2c, Supporting Information), along with minimal traces of Cs_4PbBr_6 until the latter phase is no longer directly observable in samples prepared with 12% H_2O (Figure 1f). In the samples containing 9% and 12% H_2O there is a strong decrease in the signal at 120 cm^{-1} which is fundamental for the structural stability of the Cs_4PbBr_6, and a broadening of the peaks below 100 cm^{-1} with an increase in the signal due to the presence of $CsPbBr_3$, suggesting the breakage of the isolated octahedra and the predominance of a 3D structure (connected octahedra).[42] A broad Raman feature observed in the 150–200 cm^{-1} region is likely due to the overlap of Pb—Br stretching modes and low-frequency lattice vibrations (marked with vertical line). Additionally, such broadening can be attributed to structural disorder or phase mixing, where the coexistence of $CsPbBr_3$ and Cs_4PbBr_6 leads to overlapping vibrational contributions and increased inhomogeneity in the local lattice environment. Taking this into consideration, together with the broadening of FWHM reported in Figure S1e (Supporting Information), we suggest that Cs_4PbBr_6 is present as small or structurally disordered crystallites: such domains remain detectable by XRD but yield only weak, broadened, and partially overlapped Raman features. To clarify the attribution of the Raman features across the series, we have included a summary table (Table S2, Supporting Information) listing the characteristic vibrational ranges associated with each phase (Cs_4PbBr_6 and $CsPbBr_3$). All samples display a microscopic dominant phase, except for the 6% H_2O condition, which presents spectral contributions from both Cs_4PbBr_6 and $CsPbBr_3$, indicating a heterogeneous composition with coexisting 0D and 3D structural domains.

In order to gain insight into the mechanism that leads to the modulation of the perovskite phase with H_2O, the optical and structural properties of the supernatant of the different solutions, collected after the powder precipitation, were analyzed. The analysis of supernatant is fundamental to understanding the reaction mechanism, as its composition reflects the chemical equilibrium and solubility dynamics during transformation. Changes in ionic concentrations in the supernatant can indeed indicate the formation of intermediate complexes or coordination equilibria involved in the phase transition. This also provides insight into defect formation in the final 3D phase, such as halide vacancies or off-stoichiometry, potentially linked to selective component leaching. Overall, supernatant analysis can provide important information on the connection between solution chemistry and solid-state evolution, supporting the transformation pathway

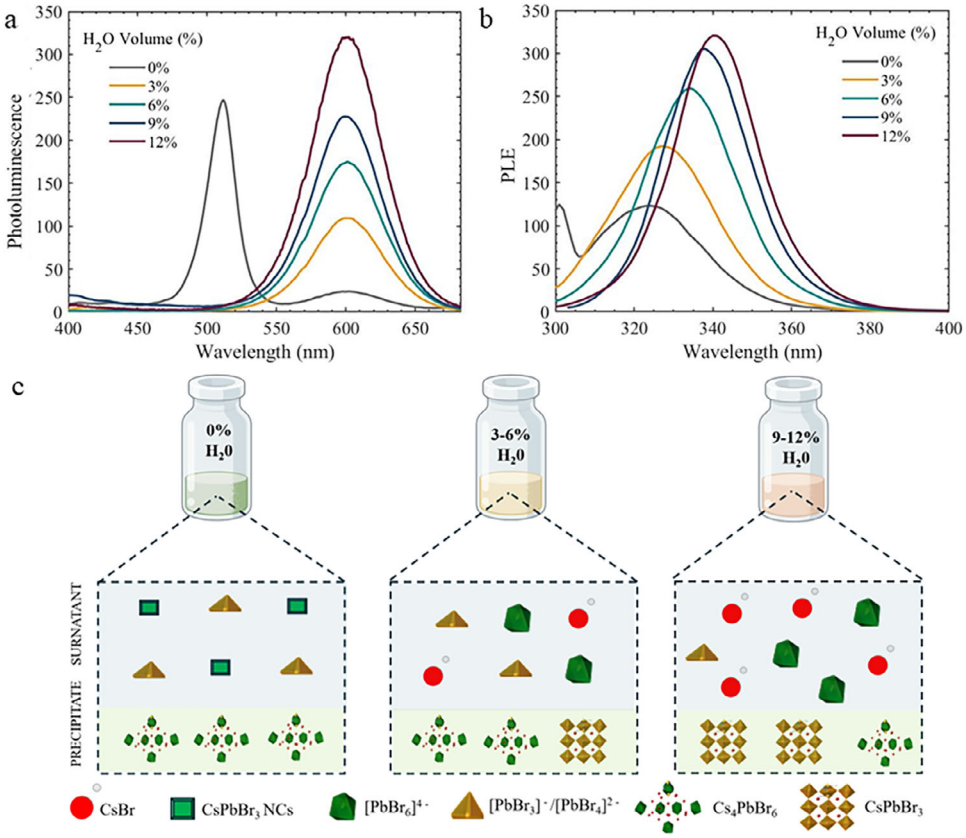

Figure 2. a)PL and b) PLE spectra of the supernatant of Cs_4PbBr_6 powders with different volumes of H_2O in precipitation. c) Precipitation process and modulation mechanism mediated by water in Cs_4PbBr_6 powder.

and offering a more complete view of the synthesis and material quality. In **Figure** 2a the PL spectra of supernatant solutions are reported. The supernatant obtained by precipitating perovskite powder with pure THF shows two peaks, centred at 520 and at 600 nm. Upon the addition of an incremental amount of H_2O in the antisolvent, the peak at 600 nm gradually increases in intensity until it reaches a maximum, while the peak at 520 nm disappears. The peak at 520 nm can be attributed to the presence of nanometres-sized aggregates of $CsPbBr_3$ in the supernatant solution, which can be decomposed by the inclusion of H_2O in the antisolvent mixture, seen as a reduction of the emission (Figure S3a, Supporting Information). The peak at 600 nm can be attributed instead to a combination of polybrominated lead species, $[PbBr_3]^-$ and $[PbBr_4]^{2-}$ which gradually increases with the presence of water in the antisolvent. Notably, these two species exhibit emission at 604 and 560 nm in solution, with absorption peak at 306 and 343 nm for $[PbBr_3]^-$ and $[PbBr_4]^{2-}$ respectively.[30,43] Besides emission spectra, we collected also the photoluminescence excitation (PLE) spectra of the supernatant which featured a peak initially centred at ≈325 nm for the sample without H_2O, gradually redshifting with increasing water content in the antisolvent, suggesting the formation of higher-order lead polybromide complexes, such as $[PbBr_5]^{3-}$ or $[PbBr_6]^{4-}$ in the supernatant solutions (Figure 2b).[44,45] Their presence is also evinced also by the absorption spectra, where the addition of H_2O to the antisolvent results in the appearance of a more intense tail (310–360 nm), which can be attributed to these lead polybromide complexes[24] (Figure 3b). Scanning electron microscopy (SEM), High-Angle Annular Dark-Field (HAADF)-Scanning Transmission Electron Microscopy (STEM) images coupled with the Energy Dispersive X-ray Spectrometer (EDX) mapping for selected supernatant samples are reported and discussed in Figures S3–S5 and Table S3 (Supporting Information).

Based on the optical and morphological/compositional characterization of the supernatant we propose the precipitation mechanism for perovskite powders sketched in Figure 2c. According to the structural analysis, in the absence of water, the precipitated perovskite is in the Cs_4PbBr_6 phase with CsBr contamination. Consistently, in the supernatant of this sample, unreacted $PbBr_2$ with emission species of $[PbBr_3]^-$ and $[PbBr_4]^{2-}$ are present, along with nanometres-sized aggregates of $CsPbBr_3$. The inclusion of H_2O in the antisolvent results in a competitive reaction in the final product. The chemical deprivation and dissolution of CsBr from the precursors' solution, induced by the presence of H_2O in the antisolvent, gradually induce the transition of the 0D Cs_4PbBr_6 phase into the 3D $CsPbBr_3$ phase in the precipitate, following the reaction reported as (1). Simultaneously, the supernatant becomes enriched with Cs^+ and Br^- ions, where the excess of Br^- ions promotes the formation of polybrominated species at higher concentrations compared to the 0% H_2O precipitation (reaction 2). For H_2O > 6%, a third mechanism dominates the reaction (3), involving the direct degradation of Cs_4PbBr_6 into

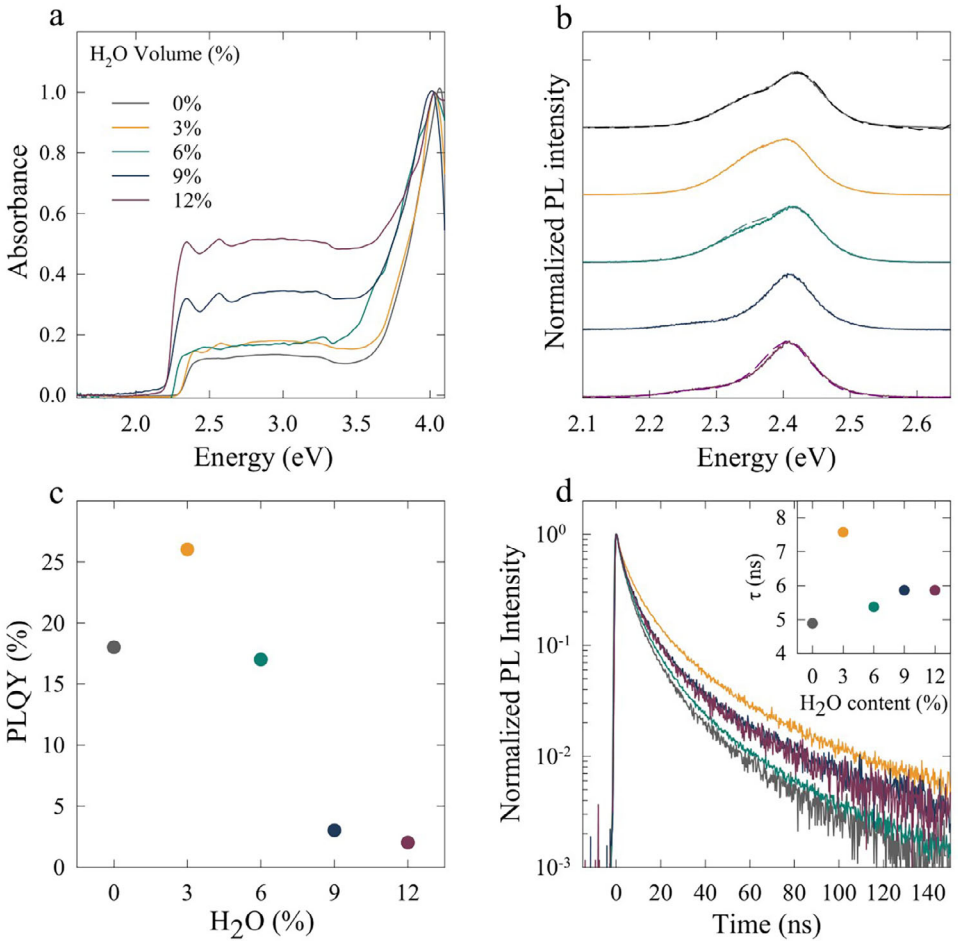

Figure 3. a) Normalized absorption, b) and PL spectra, c) PL quantum yield, and d) PL decay traces of Cs_4PbBr_6 powder with increasing amount of water (from 0 to 12%). Continuous and dashed PL spectra in (b) were excited at 3.2 and 4.0 eV respectively. PL spectra are shifted vertically for clarity. The inset in (d) shows the effective lifetimes of Cs_4PbBr_6 powder extracted as the time after which the PL intensity decreased by a factor e. The same color code applies throughout the figure.

a final product primarily composed of $CsPbBr_3$ rather than Cs_4PbBr_6 (1). This process leads to a reduced yield (Table S4, Supporting Information) and a significant presence of $[PbBr_6]^{4-}$ in the supernatant.

$$Cs_4PbBr_6 + H_2O \rightarrow 3CsBr + CsPbBr_3 \quad (1)$$

$$PbBr_3^- + Br^- \rightleftharpoons PbBr_4^{2-}\ PbBr_4^{2-} + 2Br^- \rightleftharpoons PbBr_6^{4-} \quad (2)$$

$$Cs_4PbBr_6(s) \rightleftharpoons 4Cs^+ + PbBr_6^{4-} \quad (3)$$

The optical absorption spectra of powders with increasing amount of H_2O in the antisolvent (**Figure 3a**) were obtained from the reflectance spectra measured with an integrating sphere using the Kubelka Munk method.[46] Two main characteristic features can be found in the absorption spectra, namely a narrow peak at 4.02 eV that can be attributed to the Cs_4PbBr_6 0D phase[47] and a characteristic extended band with absorption edge at 2.40 eV that is characteristic of the $CsPbBr_3$ (3D phase).[48] The relative contribution of those features to the absorption spectra varies in the different samples and with increasing H_2O in the antisolvent, indicating the gradual conversion of Cs_4PbBr_6 into $CsPbBr_3$ phase, which is also in accordance with the Raman and XRD analysis (Figure 1). The observation of the absorption contribution by $CsPbBr_3$ in the spectrum of the nominally anhydrous Cs_4PbBr_6 0D material confirms the partial spontaneous interphase conversion observed previously.[27,49] Moreover, the absorbance peak at 2.40 eV shows a clear and consistent monotonic peak broadening trend with increasing H_2O volume percentage in the antisolvent mixture (Figure S6a, Supporting Information). This trend highlights the gradual modification in sample composition and crystalline quality as the phase transition progresses. Additionally, the ratio of the integrated absorbance areas between 2.2–2.5 and 3.9–4.1 eV steadily increases with H_2O content, clearly supporting the progressive transformation from Cs_4PbBr_6 to $CsPbBr_3$ (Figure S6b, Supporting Information). The PL spectra of all samples (Figure 3b, continuous and dashed lines respectively) excited at 3.2 and 4 eV, that is below and above the bandgap energy of the Cs_4PbBr_6 phase, show a substantially identical single peak at 2.40 eV, consistent with $CsPbBr_3$ emission with a weak low-energy shoulder at 2.31 eV ascribed to $CsPbBr_3$ excitons trapped in shallow defects likely associated with halide

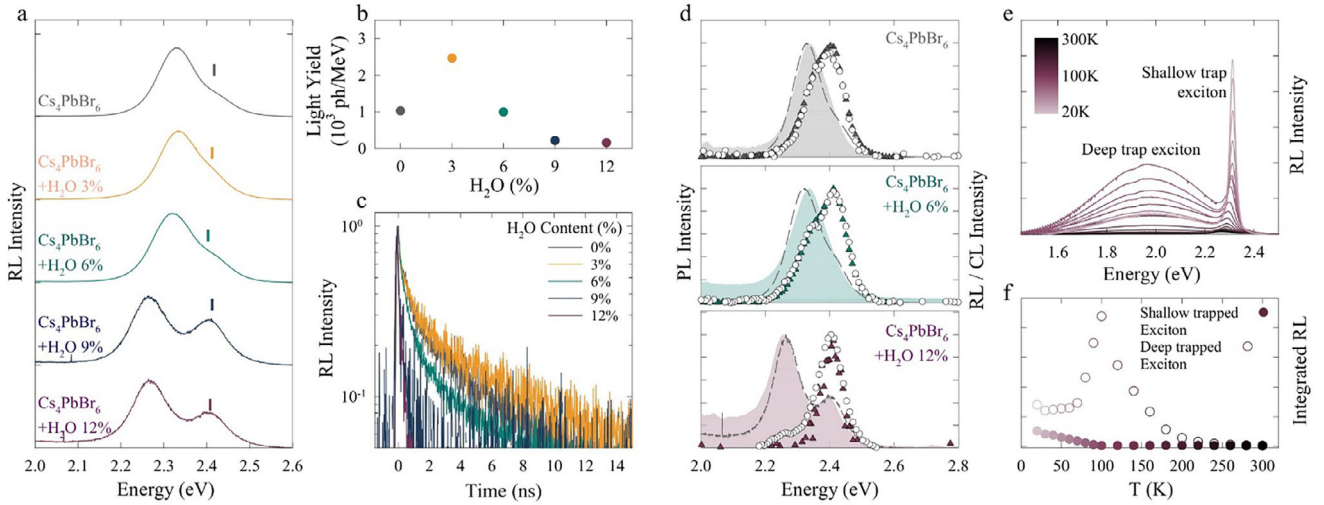

Figure 4. a) Normalized RL spectra of Cs_4PbBr_6 powders with increasing amount of water (from 0 to 12%, vertically shifted for clarity). b) LY of Cs_4PbBr_6 powders purified with increasing amount of water measured in comparison with BGO powder in the same conditions (X-ray 20 kV irradiation) and c) respective RL decay traces. d) Comparison between PL spectra collected using synchrotron excitation at 10 eV (colored triangles) and 3 eV (white circles), and CL spectra (shaded area) of Cs_4PbBr_6 powders purified with increasing amount of water. RL spectra of the same samples are reported as dashed lines for clarity. e) RL spectra collected as a function of temperature for the Cs_4PbBr_6 powder samples purified with 12% of water. f) Integrated intensity of the shallow trapped (filled circles) and deep trapped exciton (hollow circles) components as a function of temperature.

vacancies.[50] Those halide vacancies might be created by the release of CsBr in the supernatant during the Cs_4PbBr_6 to $CsPbBr_3$ conversion (see sketch in Figure 2). The relative intensity of this shoulder is constant for H_2O up to 6%, while it drastically decreases for higher water quantities. This trend is, however, accompanied by a substantial decrease of the PLQY of the perovskite powders (Figure 3c) that follows a non-monotonic trend with the water content, with an initial increase from $\Phi_{PL} = 17\%$ to $\Phi_{PL} = 27\%$ followed by a substantial decrease to less than 3% at 12% of H_2O. The initial increase in Φ_{PL}, corroborated by the longer corresponding PL decay time (Figure 3d) suggests that a tiny amount of water in the antisolvent can have a beneficial effect on the optical properties of the resulting perovskite powder, leading to a partial conversion of the 0D to 3D phases and reduced nonradiative losses for $CsPbBr_3$ excitons. A higher amount of water, however, leads to an overall reduction of Φ_{PL}, likely due to nonradiative recombination of both band edge and shallow trapped excitons. Deeper insights into the recombination process are provided by the scintillation experiments discussed below.

Given the recent interest in lead halide perovskites for scintillation radiation detection, we investigated the emission properties of our 0D–3D sample under ionizing excitation. The RL spectra under X-irradiation (average energy 10 keV) of the powders with increasing % of H_2O are shown in **Figure** 4a. The corresponding PL peak energies are marked by a vertical line. In all cases, RL shows a high energy shoulder centred at 2.40 eV with negligible spectral shift coinciding with PL and a main peak in the 2.26–2.33 eV region, resonant with the defect emission, which is minor under optical excitation and now dominates RL. The branching ratio between the two emissions does not seem to depend significantly on the amount of H_2O used in the processing, while their spectral separation essentially doubles from ≈90 to 160 meV suggesting that defects become gradually deeper in samples with larger 3D phase content. Consistently with the PL results, the scintillation yield (or light yield (LY), expressed as the number of emitted photons per energy deposited) follow a similar trend. As shown in Figure 4b, LY was measured by direct comparison with bismuth germanate powder (BGO) (LY∼9000 ph MeV^{-1}).[51,52] The LY initially increases compared to the anhydrous sample but gradually decreases at higher H_2O contents, confirming optical spectroscopy observations that defect-related non-radiative losses significantly impact the emission efficiency. The RL decay traces at room-temperature agree with the *cw* data (Figure 4c), showing slower RL decay kinetics for 3% H_2O followed by a substantial nonradiative acceleration for the lower LY samples. We noticed that for all systems the RL kinetics is markedly faster than the corresponding PL, which agrees with the reported multiexcitonic character of scintillation in nanostructures.[53,54,55] The substantial change in the spectral shape of RL compared to PL may indicate a higher probability of trapping under ionizing excitation, or that this leads to a different population of excited states, similar to what was recently observed in $CsPbBr_3$ NCs.[50,53,56] To investigate this further, we performed PL and CL measurements that reproduce the excitation by fast electrons following the primary photoelectric interaction event with X-rays (Figure 4d). Interestingly, we found that the PL spectrum retains the same shape dominated by free exciton emission from the $CsPbBr_3$ phase both under UV excitation at 3.5 eV and under synchrotron light excitation at 10 eV, corresponding to more than 2.5 times the bandgap of both 0D and 3D phases. In contrast, the CL spectrum excited by electrons at 7 keV follows the RL spectrum. This reinforces the scenario that free charges are more likely to localize in shallow defect states, while optical excitation, although high-energy, produces predominantly band-edge excitons. RL measurements as a function of temperature confirm this scenario showing the gradual intensification of the shallow defect RL (2.26 eV) and the emergence of a further broad RL band at 1.98 eV with decreasing temperature that is absent in the cryogenic PL and

is ascribed to the recombination of deep stable traps that are completely quenched in ambient conditions. In agreement with recent observations in $CsPbBr_3$ NCs,[50,56,57,58] at T = 20 K the broad defect RL persists for minutes over time after irradiation and shows strong intensification upon warming the sample to ≈100 K, thus further confirming its origin from stable deep trap states that require thermal budget to detrap to emissive intragap defects (Figure 4e,f).

3. Conclusion

In conclusion, we explored the emission properties of 0D–3D lead halide hybrid perovskites under ionizing excitation, elucidating the role of defect states in scintillation mechanisms. Our synthesis approach allowed for precise control of the $CsPbBr_3/Cs_4PbBr_6$ phase ratio, demonstrating that the introduction of water selectively promotes the formation of the 3D phase at the expense of the 0D phase. The phase composition of $CsPbBr_3/Cs_4PbBr_6$ was confirmed through a comprehensive set of characterizations, including Raman spectroscopy, XRD, and optical analyses of the supernatant and of the final powder. RL spectra revealed two key emission features: an excitonic peak at 2.40 eV and a dominant defect-related emission in the 2.26–2.33 eV range, which intensifies under X-ray excitation. The progressive deepening of defect states, as indicated by an increasing spectral shift with hydration, correlates with variations in scintillation yield, which initially improves but declines at high water content due to enhanced non-radiative losses. CL measurements confirmed that ionizing excitation favors charge localization in shallow traps, while PL remains dominated by band-edge excitonic recombination. Additionally, temperature-dependent RL studies identified a deep trap emission at 1.98 eV at cryogenic temperatures, which persists post-irradiation, further supporting the presence of thermally activated recombination pathways. These findings provide crucial insights into the interplay between structural phase composition, defect states, and scintillation in hybrid perovskites. Overall, our results highlight the potential of controlled phase engineering to optimize perovskite-based scintillators for radiation detection applications. Future studies should further investigate defect passivation strategies and explore alternative synthesis routes to enhance light yield and minimize non-radiative losses.

Supporting Information

Supporting Information is available from the Wiley Online Library or from the author.

Acknowledgements

M.C. and F.C. contributed equally to this work. The research activities leading to this work were supported by the National Institute of Nuclear Physics – INFN (SHINE project). This work was funded by Horizon Europe EIC Pathfinder program through project 101098649 – UNICORN, by the European Union -Next Generation EU, Mission 4 Component 1 CUP H53D23004670006, and through the Italian Ministry of University and Research under PNRR—M4C2-I1.3 Project PE_00000019 "HEAL ITALIA". This research is funded and supervised by the Italian Space Agency (Agenzia Spaziale Italiana, ASI) in the framework of the Research Day "Giornate della Ricerca Spaziale" initiative through the contract ASI N. 2023-4-U.0t A.G and A.R. acknowledge PNRR MUR project: "Integrated Infrastructure Initiative in Photonic and Quantum Sciences" – I-PHOQS (IR0000016). E.F. acknowledges financial support from PNRR MUR project ECS_00000033_ECOSISTER. The authors also acknowledge DESY and the European Community support for measurements at HASYLAB (P66, Superlumi beamline) under Contract I-20230891. This work was partly funded by the research project: "nuovi Concetti, mAteriali e tecnologie per l'iNtegrazione del fotoVoltAico negli edifici in uno scenario di generazione diffuSa" [CANVAS], funded by the Italian Ministry of the Environment and the Energy Security, through the Research Fund for the Italian Electrical System (type-A call, published on G.U.R.I. n. 192 on 18-08-2022), CUP B53C22005670005. A.M., D.A., and C.G gratefully thank F. Baldassarre for his technical assistance. M.C., N.V., A.G., R.M. and A.R. gratefully thank Sonia Carallo for technical support.

Open access publishing facilitated by Consiglio Nazionale delle Ricerche, as part of the Wiley - CRUI-CARE agreement.

Conflict of Interest

The authors declare no conflict of interest.

Data Availability Statement

The data that support the findings of this study are available from the corresponding author upon reasonable request.

Keywords

excitons, low dimensionality, optical properties, perovskite, scintillator

Received: May 23, 2025
Revised: September 5, 2025
Published online: October 10, 2025

[1] Y. Wang, M. I. Dar, L. K. Ono, T. Zhang, M. Kan, Y. Li, L. Zhang, X. Wang, Y. Yang, X. Gao, Y. Qi, M. Grätzel, Y. Zhao, *Science* **2019**, *365*, 591.
[2] Y. He, M. Petryk, Z. Liu, D. G. Chica, I. Hadar, C. Leak, W. Ke, I. Spanopoulos, W. Lin, D. Y. Chung, B. W. Wessels, Z. He, M. G. Kanatzidis, *Nat. Photonics* **2021**, *15*, 36.
[3] H. Lin, C. Zhou, Y. Tian, T. Siegrist, B. Ma, *ACS Energy Lett.* **2018**, *3*, 54.
[4] E. Shi, Y. Gao, B. P. Finkenauer, Akriti, A. H. Coffey, L. Dou, *Chem. Soc. Rev.* **2018**, *47*, 6046.
[5] P. Gao, A. R. Bin Mohd Yusoff, M. K. Nazeeruddin, *Nat. Commun.* **2018**, *9*, 5028.
[6] M. Liu, J. Zhao, Z. Luo, Z. Sun, N. Pan, H. Ding, X. Wang, *Chem. Mater.* **2018**, *30*, 5846.
[7] S. Ullah, J. Wang, P. Yang, L. Liu, S. E. Yang, T. Xia, H. Guo, Y. Chen, *Mater. Adv.* **2021**, *2*, 646.
[8] Q. Xu, X. Wang, H. Zhang, W. Shao, J. Nie, Y. Guo, J. Wang, X. Ouyang, *ACS Appl. Electron. Mater.* **2020**, *2*, 879.
[9] H. Wang, X. Zhang, Q. Wu, F. Cao, D. Yang, Y. Shang, Z. Ning, W. Zhang, W. Zheng, Y. Yan, S. V. Kershaw, L. Zhang, A. L. Rogach, X. Yang, *Nat. Commun.* **2019**, *10*, 665.
[10] M. I. Saidaminov, J. Almutlaq, S. Sarmah, I. Dursun, A. A. Zhumekenov, R. Begum, J. Pan, N. Cho, O. F. Mohammed, O. M. Bakr, *ACS Energy Lett.* **2016**, *1*, 840.

[11] H. Zhang, Q. Liao, Y. Wu, J. Chen, Q. Gao, H. Fu, *Phys. Chem. Chem. Phys.* **2017**, *19*, 29092.
[12] X. Wu, Q. Zhou, H. Wu, X. Du, G. Niu, G. Liang, Q. Hu, J. Xiao, *J. Phys. Chem. C* **2021**, *125*, 26619.
[13] Y. Li, W. Shao, L. Chen, J. Wang, J. Nie, H. Zhang, S. Zhang, R. Gao, X. Ouyang, X. Ouyang, Q. Xu, *NPG Asia Mater.* **2021**, *13*, 40.
[14] A. Giuri, A. C. Chekkallur, M. Calora, R. Mastria, L. Martinazzoli, E. Auffray, S. K. Padmanabhan, S. Carturan, S. Moretto, G. Quarta, L. Calcagnile, M. Polo, A. Quaranta, A. Maffezzoli, A. P. Caricato, A. Rizzo, C. Esposito Corcione, *Adv. Funct. Mater.* **2025**, *35*, 2417653.
[15] Y. Zhang, L. Sinatra, E. Alarousu, J. Yin, A. M. El-Zohry, O. M. Bakr, O. F. Mohammed, *J. Phys. Chem. C* **2018**, *122*, 6493.
[16] W. Sun, Y. T. Hung, W. T. Huang, R. S. Liu, W. Zhou, *Cryst. Growth Des.* **2024**, *24*, 545.
[17] Q. A. Akkerman, S. Park, E. Radicchi, F. Nunzi, E. Mosconi, F. De Angelis, R. Brescia, P. Rastogi, M. Prato, L. Manna, *Nano Lett.* **2017**, *17*, 1924.
[18] Z. Bao, H. D. Chiu, W. Wang, Q. Su, T. Yamada, Y. C. Chang, S. Chen, Y. Kanemitsu, R. J. Chung, R. S. Liu, *J. Phys. Chem. Lett.* **2020**, *11*, 10196.
[19] B. Kang, K. Biswas, *J. Phys. Chem. Lett.* **2023**, *14*, 10378.
[20] J. Yin, H. Yang, K. Song, A. M. El-Zohry, Y. Han, O. M. Bakr, J. L. Brédas, O. F. Mohammed, *J. Phys. Chem. Lett.* **2018**, *9*, 5490.
[21] B. M. Benin, D. N. Dirin, V. Morad, M. Wörle, S. Yakunin, G. Rainò, O. Nazarenko, M. Fischer, I. Infante, M. V. Kovalenko, *Angew. Chem., Int. Ed.* **2018**, *57*, 11329.
[22] J. Yin, P. Maity, M. De Bastiani, I. Dursun, O. M. Bakr, J. L. Brédas, O. F. Mohammed, *Sci. Adv.* **2017**, *3*, 1701793.
[23] D. Sharma, S. K. Sharma, *Opt. Mater.* **2024**, *157*, 116250.
[24] A. Ray, D. Maggioni, D. Baranov, Z. Dang, M. Prato, Q. A. Akkerman, L. Goldoni, E. Caneva, L. Manna, A. L. Abdelhady, *Chem. Mater.* **2019**, *31*, 7761.
[25] X. Liu, W. Xie, Y. Lu, X. Wang, S. Xu, J. Zhang, *J. Mater. Chem. C* **2022**, *10*, 762.
[26] L. Wu, H. Hu, Y. Xu, S. Jiang, M. Chen, Q. Zhong, D. Yang, Q. Liu, Y. Zhao, B. Sun, Q. Zhang, Y. Yin, *Nano Lett.* **2017**, *17*, 5799.
[27] F. Palazon, C. Urso, L. De Trizio, Q. Akkerman, S. Marras, F. Locardi, I. Nelli, M. Ferretti, M. Prato, L. Manna, *ACS Energy Lett.* **2017**, *2*, 2445.
[28] Q. Zhou, X. Zhao, Y. Jiang, J. Zhou, Z. Liu, K. Pan, *ACS Appl. Nano Mater.* **2025**, *8*, 2046.
[29] S. J. Yoon, K. G. Stamplecoskie, P. V. Kamat, *J. Phys. Chem. Lett.* **2016**, *7*, 1368.
[30] K. Oldenburg, A. Vogler, *Z. Naturforsch. B* **1993**, *48*, 1519.
[31] A. Altomare, N. Corriero, C. Cuocci, A. Falcicchio, A. Moliterni, R. Rizzi, *J. Appl. Crystallogr.* **2015**, *48*, 598.
[32] S. Gražulis, A. Daškevič, A. Merkys, D. Chateigner, L. Lutterotti, M. Quirós, N. R. Serebryanaya, P. Moeck, R. T. Downs, A. Le Bail, *Nucleic Acids Res.* **2012**, *40*, D420.
[33] C. de Weerd, J. Lin, L. Gomez, Y. Fujiwara, K. Suenaga, T. Gregorkiewicz, *J. Phys. Chem. C* **2017**, *121*, 19490.
[34] C. A. López, C. Abia, M. C. Alvarez-Galván, B. K. Hong, M. V. Martínez-Huerta, F. Serrano-Sánchez, F. Carrascoso, A. Castellanos-Gómez, M. T. Fernández-Díáz, J. A. Alonso, *ACS Omega* **2020**, *5*, 5931.
[35] M. S. Kirschner, B. T. Diroll, P. Guo, S. M. Harvey, W. Helweh, N. C. Flanders, A. Brumberg, N. E. Watkins, A. A. Leonard, A. M. Evans, M. R. Wasielewski, W. R. Dichtel, X. Zhang, L. X. Chen, R. D. Schaller, *Nat. Commun.* **2019**, *10*, 504.
[36] D. L. Bish, S. A. Howard, *J. Appl. Cryst.* **1988**, *21*, 86.
[37] A. Altomare, C. Cuocci, G. D. Gatta, A. Moliterni, R. Rizzi, *EMU Notes Miner.* **2017**, *19*, 79.
[38] A. Altomare, C. Cuocci, C. Giacovazzo, A. Moliterni, R. Rizzi, N. Corriero, A. Falcicchio, *J. Appl. Crystallogr.* **2013**, *46*, 1231.
[39] J. Satta, C. Melis, C. M. Carbonaro, A. Pinna, M. Salado, D. Salazar, P. C. Ricci, *J. Materiomics* **2021**, *7*, 127.
[40] Z. Qin, S. Dai, V. G. Hadjiev, C. Wang, L. Xie, Y. Ni, C. Wu, G. Yang, S. Chen, L. Deng, Q. Yu, G. Feng, Z. M. Wang, J. Bao, *Chem. Mater.* **2019**, *31*, 9098.
[41] O. Yaffe, Y. Guo, L. Z. Tan, D. A. Egger, T. Hull, C. C. Stoumpos, F. Zheng, T. F. Heinz, L. Kronik, M. G. Kanatzidis, J. S. Owen, A. M. Rappe, M. A. Pimenta, L. E. Brus, *Phys. Rev. Lett.* **2017**, *118*, 136001.
[42] A. Noculak, S. C. Boehme, M. Aebli, Y. Shynkarenko, K. M. McCall, M. V. Kovalenko, *Helv. Chim. Acta* **2021**, *104*, 2000222.
[43] J. S. Manser, M. I. Saidaminov, J. A. Christians, O. M. Bakr, P. V. Kamat, *Acc. Chem. Res.* **2016**, *49*, 330.
[44] S. Rahimnejad, A. Kovalenko, S. M. Forés, C. Aranda, A. Guerrero, *ChemPhysChem* **2016**, *17*, 2795.
[45] E. Radicchi, F. Ambrosio, E. Mosconi, A. A. Alasmari, F. A. S. Alasmary, F. De Angelis, *J. Phys. Chem. B* **2020**, *124*, 11481.
[46] P. Kubelka, F. Munk, *Tech. Phys.* **1931**, *12*, 12.
[47] L. Wang, H. Liu, Y. Zhang, O. F. Mohammed, *ACS Energy Lett.* **2020**, *5*, 87.
[48] C. Y. Huang, C. C. Wu, C. L. Wu, C. W. Lin, *ACS Omega* **2019**, *4*, 8081.
[49] Y. Su, Q. Zeng, X. Chen, W. Ye, L. She, X. Gao, Z. Ren, X. Li, *J. Mater. Chem. C* **2019**, *7*, 7548.
[50] M. L. Zaffalon, F. Cova, M. Liu, A. Cemmi, I. Di Sarcina, F. Rossi, F. Carulli, A. Erroi, C. Rodà, J. Perego, A. Comotti, M. Fasoli, F. Meinardi, L. Li, A. Vedda, S. Brovelli, *Nat. Photonics* **2022**, *16*, 860.
[51] W. Drozdowski, A. J. Wojtowicz, S. M. Kaczmarek, M. Berkowski, *Phys. B* **2010**, *405*, 1647.
[52] N. Yawai, W. Chewpraditkul, C. Wanarak, M. Nikl, W. Ratanatongchai, *Opt. Mater.* **2014**, *36*, 2030.
[53] A. Fratelli, M. L. Zaffalon, E. Mazzola, D. N. Dirin, I. Cherniukh, C. Otero-Martínez, M. Salomoni, F. Carulli, F. Rossi, F. Meinardi, L. Gironi, L. Manna, M. V. Kovalenko, S. Brovelli, *Adv. Mater.* **2025**, *37*, 2413182.
[54] K. Děcká, F. Pagano, I. Frank, N. Kratochwil, E. Mihóková, E. Auffray, V. Čuba, *J. Mater. Chem. C* **2022**, *10*, 12836.
[55] M. L. Zaffalon, A. Fratelli, Z. Li, F. Bruni, I. Cherniukh, F. Carulli, S. Brovelli, *Adv. Mater.* **2025**, *37*, 2500846.
[56] F. Cova, A. Erroi, M. L. Zaffalon, A. Cemmi, I. Di Sarcina, J. Perego, A. Monguzzi, A. Comotti, F. Rossi, F. Carulli, S. Brovelli, *Nano Lett.* **2024**, *24*, 905.
[57] C. Rodà, M. Fasoli, M. L. Zaffalon, F. Cova, V. Pinchetti, J. Shamsi, A. L. Abdelhady, M. Imran, F. Meinardi, L. Manna, A. Vedda, S. Brovelli, *Adv. Funct. Mater.* **2021**, *31*, 2104879.
[58] A. Erroi, F. Carulli, F. Cova, I. Frank, M. L. Zaffalon, J. Llusar, S. Mecca, A. Cemmi, I. Di Sarcina, F. Rossi, L. Beverina, F. Meinardi, I. Infante, E. Auffray, S. Brovelli, *ACS Energy Lett.* **2024**, *9*, 2333.